



Article

Advancing FDM 3D Printing Simulations: From G-Code Conversion to Precision Modelling in Abaqus

Taoufik Hachimi ^{1,*}, Fouad Ait Hmazi ¹, Fatima Ezzahra Arhouni ¹, Hajar Rejdali ², Yahya Riyad ² and Fatima Majid ¹

¹ Laboratory of Nuclear, Atomic, Molecular, Mechanical, and Energetic Physics, University Chouaib Doukkali, El Jadida 24000, Morocco

² Laboratory of Engineering Sciences for Energy (LabSIE), University Chouaib Doukkali, El Jadida 24000, Morocco

* Correspondence: Hachtaoufik@gmail.com; Tel.: +212-676067714

Abstract

This study presents a newly developed program that seamlessly converts G-code into formats compatible with Abaqus, enabling precise finite element simulations for FDM 3D printing. The tool operates on a two-pronged framework: a mathematical model incorporating key print parameters (layer thickness, extrusion temperature, print speed, and raster width) and a shape generator managing geometric parameters (fill density, pattern, and raster orientation). Initially, a predefined virtual section, based on predetermined dimensions, enhanced the correlation between experimental results and simulations. Subsequently, a corrected virtual section, derived from the mathematical model using the Box-Behnken methodology, improves accuracy, achieving a virtual thickness error of 1.06% and a width error of 8%. The model is validated through tensile testing of ASTM D638 specimens at 0°, 45°, and 90° orientations, using adaptive C3D4 mesh elements (0.35–0.6 mm). Results demonstrate that the corrected cross-section significantly improved simulation accuracy, reaching correlations above 95% in the elastic zone and 90% in the elastoplastic zone across all orientations. By optimizing the workflow from design to manufacturing, this program offers substantial benefits for the aerospace, medical, and automotive sectors, enhancing both the efficiency of the printing process and the reliability of simulations.



Academic Editor: Narges Dialami

Received: 12 August 2025

Revised: 27 September 2025

Accepted: 30 September 2025

Published: 16 October 2025

Citation: Hachimi, T.; Ait Hmazi, F.; Arhouni, F.E.; Rejdali, H.; Riyad, Y.; Majid, F. Advancing FDM 3D Printing Simulations: From G-Code Conversion to Precision Modelling in Abaqus. *J. Manuf. Mater. Process.* **2025**, *9*, 338. <https://doi.org/10.3390/jmmp9100338>

Copyright: © 2025 by the authors. Licensee MDPI, Basel, Switzerland. This article is an open access article distributed under the terms and conditions of the Creative Commons Attribution (CC BY) license (<https://creativecommons.org/licenses/by/4.0/>).

1. Introduction

3D printing, sometimes referred also as additive manufacturing (AM), has led to a substantial change in how we think about manufacturing processes [1–3]. This breakthrough technique permits the direct fabrication of complex geometries through virtual models [4]. In contrast to typical subtractive manufacturing processes, which require removing material to achieve a desired shape, AM creates items layer by layer, enabling unequalled design freedom and customization possibility [5–8]. This technology has altered several areas, including aerospace, medicine, and the automobile sector, making it feasible to print sophisticated components and prototypes with exceptional precision [9,10].

G-code, a programming language developed in the 1950s for computer numerical control (CNC) machine tools [11,12], plays a critical role in the 3D printing process [13]. It consists of a series of G and M commands that precisely control the movement, speed,

and activities of 3D printers during the fabrication process [14]. In the context of additive manufacturing, G-code serves as the essential bridge between digital design and physical production, translating CAD models into machine instructions for layer-by-layer material deposition [15]. For finite element analysis (FEA) tools like SIMULIA Abaqus [16,17], G-code provides the critical path information necessary to simulate the actual printing process, including thermal and mechanical behavior during fabrication [18,19].

Despite its importance, the conversion of G-code to simulation-ready models presents significant challenges. While Abaqus offers comprehensive tools for modeling various aspects of the 3D printing process—such as heat transfer, material solidification, stress analysis, and structural deformation—the accurate representation of the physical printing process remains difficult [20–22]. The mechanical response of printed specimens is highly dependent on numerous printing parameters, and G-code itself varies significantly across different 3D printers and slicing software [14]. This heterogeneity necessitates sophisticated parsing algorithms capable of extracting meaningful information from diverse G-code dialects [23]. As documented by Zouaoui et al. [18] and Brenken et al. [24], current conversion methods often fail to account for physical filament deformation during printing, resulting in simulation errors exceeding 15% in stress distribution predictions.

Several studies have attempted to address these challenges. Favaloro et al. [25] employed Digimat-AM[©] to simulate FDM processes, while Talagani et al. [26] presented one of the most advanced studies on Extrusion Deposition Additive Manufacturing (EDAM) simulations. Their work modeled deformation and residual stresses across an entire fiber-reinforced thermoplastic car chassis, incorporating progressive element activation and spatially varying material orientations to capture the inherent anisotropy of printed structures. Faria et al. [27] developed FIBR3DEmul, an open-access simulation solution for FDM machines with 3+ actuated axes, while Brenken et al. [24] extended this work by simulating the Extrusion Deposition Additive Manufacturing (EDAM) process in Abaqus to predict final deformed geometries and residual stresses. However, these approaches have limitations: Faria et al.'s [27] method focuses primarily on motion simulation without addressing corrected virtual section for filament deformation, and Brenken et al. [24] approach lacks comprehensive parameter optimization for virtual raster sections. Similarly, Zhang et al. [21] used Abaqus to examine milling temperature in titanium alloys for aerospace components, but their work did not address the fundamental challenges of G-code conversion for additive manufacturing simulations.

A critical gap exists in the current literature: no existing method simultaneously addresses accurate G-code parsing, physical filament deformation correction, and adaptive mesh generation for FDM simulations. While Molazadeh et al. [28] achieved 77% correlation between simulation and experimental results using unidirectional deposition without continuation, their approach did not incorporate corrected virtual section for filament deformation during the conversion process. Timofeeva et al. [29] emphasized the need for process simulation systems for small batch production, Zhang et al. [21] used Abaqus to examine the effect of cutting conditions on milling temperature in aerospace material. Zouaoui et al. [20] determined the correlation of 85% to 73% between the numerical model and the tensile test result via the use of a method of reinforcement of a matrix by fibers. Dallal et al. [30] recently reviewed the orientation-dependent mechanical properties of high-performance polymers like PEEK, demonstrating how raster orientation significantly affects ultimate tensile strength (73 MPa at 0° vs. 54 MPa at 90°), highlighting the critical importance of accurate geometric representation in FDM simulations. This limitation significantly affects the accuracy of stress distribution predictions, particularly in complex geometries and multi-material prints.

Despite recent advances in G-code parsing and process-aware finite-element models, two important gaps remain: (1) most conversion workflows use nominal filament cross-sections that do not reflect extrusion physics and printer settings, producing geometry errors that degrade simulation fidelity; (2) few tools offer an automated, validated pipeline from printer G-code to Abaqus with a physically calibrated filament cross-section. To address these gaps this manuscript proposes a two-module approach: (i) a mathematical model, calibrated by a Box–Behnken experimental design, to predict a corrected virtual filament section as a function of printing parameters; and (ii) a shape-generator and interface that sweeps that corrected section along the G-code toolpath and exports an Abaqus INP ready for simulation. We validate the workflow by comparing simulations to tensile experiments on ASTM D638 specimens printed at 0°, 45°, and 90° raster orientations. The main contributions are:

- A physically calibrated polynomial model for virtual filament cross-section (Box–Behnken calibration).
- A Python-based G-code → Abaqus interface and shape generator that produces mesh-ready geometry.
- A validation suite combining SEM and tensile tests to quantify geometry and mechanical fidelity.

These elements together provide an automated, experimentally anchored path from printer settings to improved FEA predictive capability for FFF parts.

2. Materials and Methods

This section details the methodology for developing and validating a G-code-to-Abaqus conversion tool. The primary objective is to establish a workflow that accurately translates physical printing parameters into numerical samples used for simulations with emphasis on correcting filament cross-section deformation and optimizing mesh generation for stress analysis. The methodology encompasses four key components: (1) monofilament section analysis (which uses oval-rectangular shape defined by length and height), experimentally analyzing the effect of printing parameters on these two dimensions using Box–Behnken experimental design to define the dimension of the virtual section used as base to create the numerical sample; (2) shape generator that follows the G-code instructions given the virtual section a path for generating; (3) integration of a fixed mesh to samples depending on complexities of the component, with mesh size ranging between 0.35 and 0.6 mm; and (4) interface has been added to facilitate communication with the user. Validation is performed by comparing the geometry of the generated sample in Abaqus with the slicer-generated geometry and conducting numerical tensile tests using both corrected and non-corrected section models (based on Hachimi et al.’s [31] approach). This validation approach confirms the tool’s reliability, enabling direct simulation of similar samples without requiring additional experimental testing.

Developing and validating a tool code for a 3D printer involves several key steps. Initially, designing an FDM specimen in CAD software and saving it as an STL file. This STL file is then sliced along with desired printing parameters, generating G-code instructions that are used both for the 3D printer to create a physical specimen and to extract the printing parameters used for calculation using a mathematical model associated with the virtual section.

The flowchart presented in Figure 1 outlines the process for developing and validating a tool-code for the integration of modern manufacturing techniques with computational analysis tools (FEA), Abaqus, to ensure that manufactured parts meet design specifications and performance criteria.

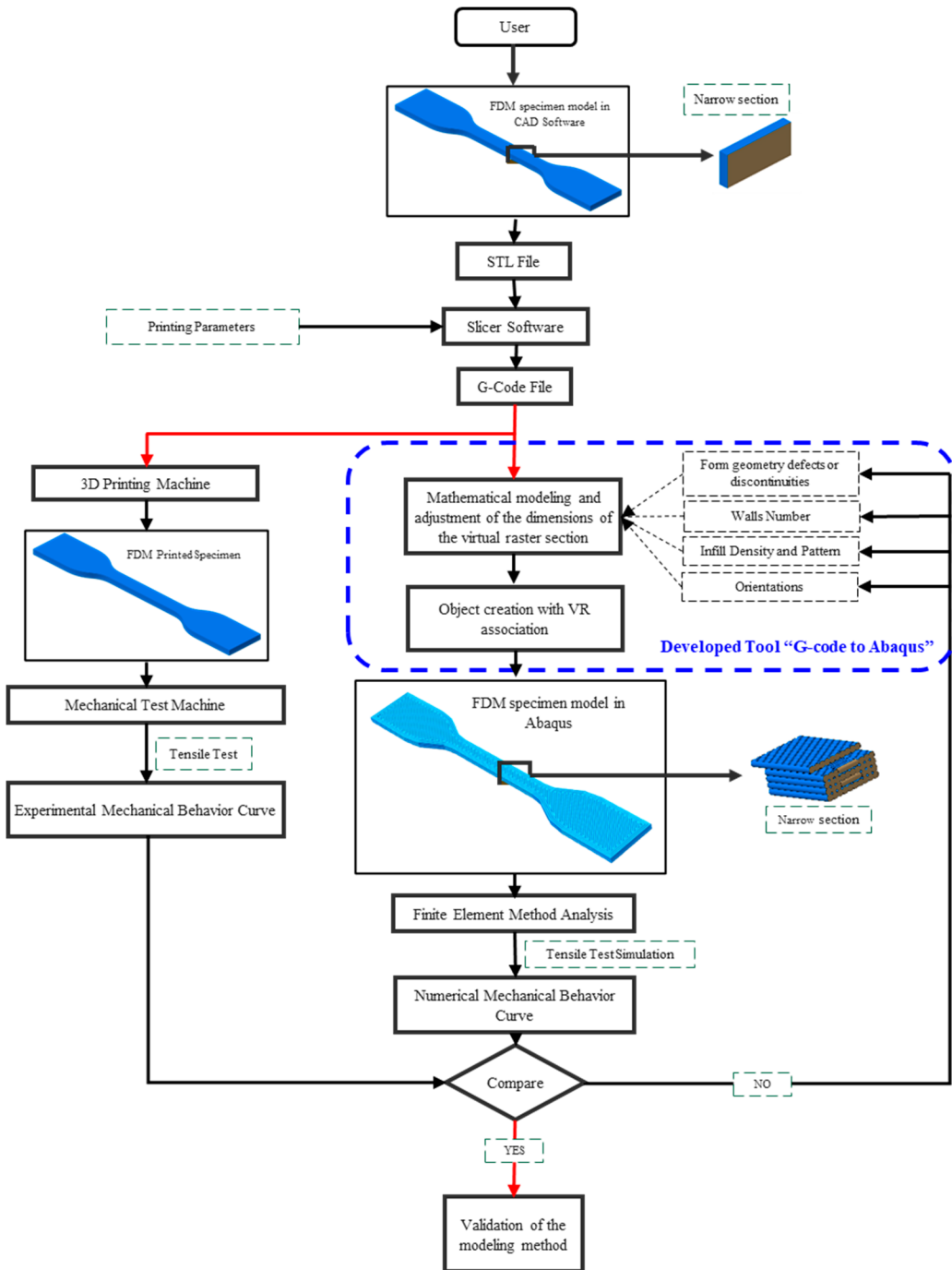


Figure 1. Flowchart of Development and Validation of G-code to Abaqus Tool.

2.1. Printing Parameter Optimization

To produce a 3D-printed test specimen with optimized mechanical behavior, precise control over multiple parameters is essential, as these parameters significantly influence the Filament section. These parameters are presented in Figure 2.

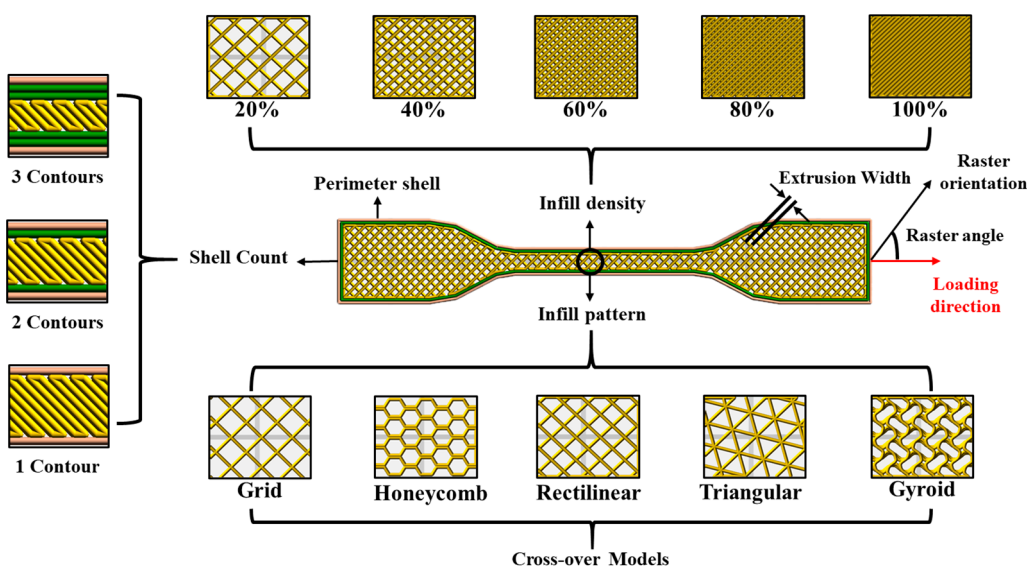


Figure 2. Printing Parameters of 3D-Printed Test Specimens.

The developed interface employs a dual-approach framework that addresses both physical and geometric aspects through a mathematical model and a shape generator, collectively managing several critical parameters. Based on Box–Behnken experimental design, the mathematical model processes printing parameters to generate corrected virtual filament cross-sections, which are then fed into the shape generator module. The shape generator uses these corrected cross-sections and link it directly to the path extracted on G-code to create a meshable 3D geometry that accurately represents the physical printed structure, including the different printing parameter. The mathematical model takes the physical parameters: layer thickness, which governs the height of each deposited layer; extrusion temperature, which controls the material's temperature during extrusion; printing speed, which determines the rate of the nozzle's movement; and raster width, which defines the width of the extruded material bead. Along with this, the shape generator controls eight geometric parameters: infill density, which sets the ratio of internal material fill; cross patterns, which define the intersecting fill geometries; raster orientation, which determines the pathway direction of material; raster angle, which sets the angle of these pathways; layer count, which defines the total number of layers; infill pattern, which selects the internal geometric pattern; perimeter count, which determines the number of outer wall layers; and print continuity, which ensures continuous deposition transitions. The overall control over physical and geometric parameters is the foundation of a sound modeling strategy, resulting in the creation of a mathematical model aimed at process printing improvement.

2.2. Numerical Specimen Generation

The filament used in 3D printing can flatten due to the combined effects of temperature and contact with the build plate, transforming its initially circular cross-section into an oval-rectangular shape. This observation aligns with measurements obtained through scanning electron microscopy, which confirm the altered geometry of the filament after deposition.

The initial virtual section geometry a circular cross-section with diameter matching the 0.4 mm nozzle was selected to reflect standard slicer assumptions and enable direct comparison with uncorrected simulation baselines. However, SEM measurements (Figure 3) revealed consistent flattening ($\text{Exp H} < \text{nozzle diameter}$) and widening ($\text{Exp L} > \text{nozzle diameter}$), motivating the need for correction.

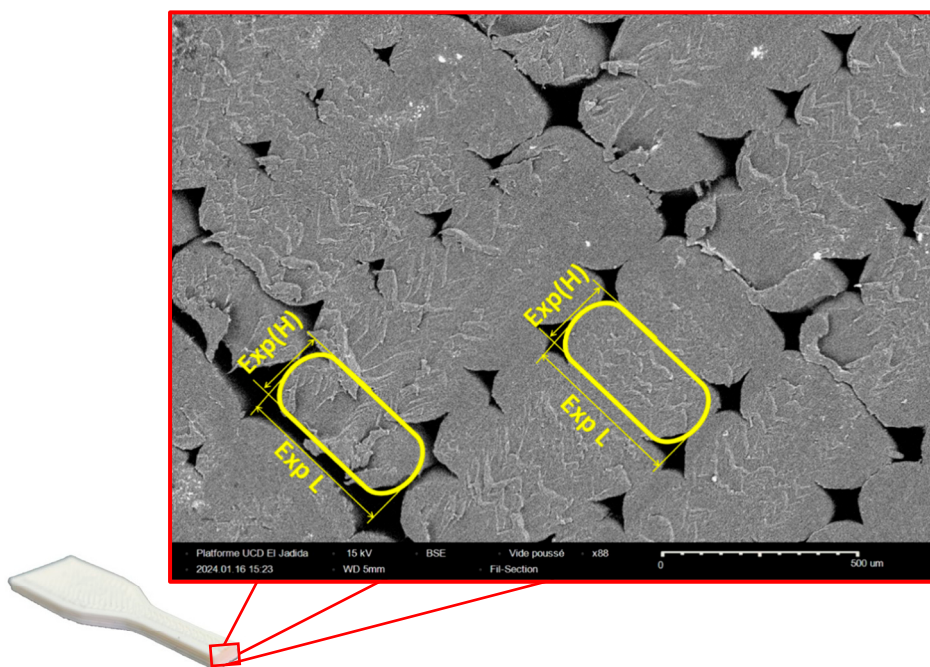


Figure 3. The shape of individual filaments is visible in a cross-section of raster layers in scanning electron microscopy (SEM).

Figure 3 illustrates the distinctive shapes of individual filaments and the area of interaction observed through the utilization of scanning electron microscopy. The dimensions of the experimental filaments, namely Experimental length (Exp L) and Experimental thickness (Exp H), were determined utilizing the Tabletop SEM model SH-5500P.

2.3. Mathematical Modeling of Virtual Raster Section

The corrected virtual section refers to the experimentally validated cross-sectional geometry of deposited filaments, which accounts for physical deformation during printing specifically, the ovalization and flattening caused by extrusion pressure, thermal softening, and layer adhesion rather than assuming an idealized circular or rectangular cross-section. This correction is derived from SEM measurements of actual printed filaments under controlled printing conditions and is calibrated using the Box–Behnken experimental design to relate printing parameters (layer thickness, raster width, temperature, speed) to final filament dimensions (virtual width and virtual thickness). The original (uncorrected) section assumes nominal slicer-defined dimensions (circular filament with diameter equal to nozzle size), which fails to capture real-world deformation observed experimentally.

To validate the corrected virtual section, we performed a series of experimental tests using a standard FlashForge FDM printer and measured the actual filament cross-sections under various printing conditions Table 1. This step focuses on building a mathematical model that relates certain manufacturing parameters to the dimensions of the virtual raster section.

This model aims to understand and predict the relationship between manufacturing parameters, such as print speed and extrusion temperature, raster width, and layer thickness, with virtual raster dimensions, such as the width and height of the deposited filament. We will use a methodology based on the Box–Behnken method design of experiment. It has 4 parameters with 3 levels. 27 pieces must be manufactured in parallelepiped form, then calculate the thickness and height for each part and divide them, respectively, by the number of threads and the number of layers (Figure 4). The Box–Behnken design was employed to investigate the effects of four process parameters layer thickness (L_t), raster

width (R_w), extrusion temperature (E_t), and print speed (P_s), on the virtual thickness and the virtual width. The experimental design and parameter settings are summarized in Table 2.

Table 1. Experimental Printing Conditions for Virtual Raster Section Validation.

Factor	Symbol	Low Level (1)	Center Level (0)	High Level (+1)
Layer thickness (mm)	L_t	0.2	0.3	0.4
Raster width (mm)	R_w	0.6	0.7	0.8
Extrusion temperature (°C)	E_t	230	240	250
Printing speed (mm/s)	P_s	10	30	50

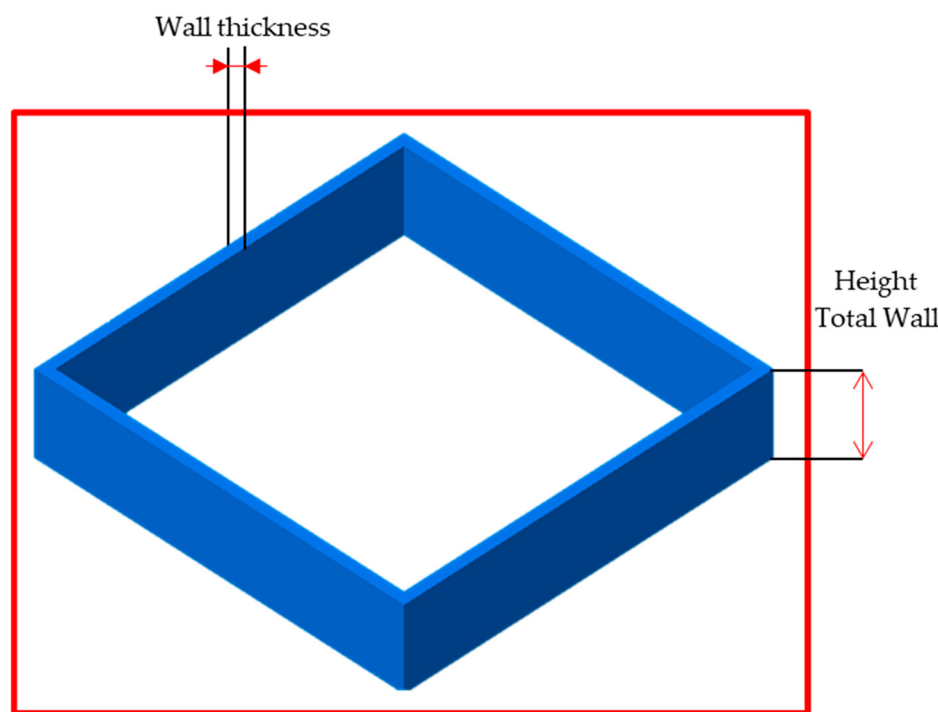


Figure 4. Box–Behnken design parallelepiped specimens for dimensional normalization.

Table 2. Box–Behnken Design Experimental Runs with Process Parameters and Dimensional Errors.

Sd	Factors				Responses			
	L_t (mm)	R_w (mm)	E_t (°C)	P_s (mm/s.)	L_t (mm)	L_t Error	R_w (mm)	R_w Error
1	0.3	0.8	250	30	0.300	0.000	0.870	0.087
2	0.3	0.6	240	10	0.296	0.013	0.586	0.023
3	0.2	0.7	230	30	0.205	0.025	0.671	0.041
4	0.3	0.7	240	30	0.302	0.007	0.670	0.043
5	0.2	0.7	240	10	0.200	0.000	0.707	0.010
6	0.3	0.7	240	30	0.300	0.000	0.670	0.043
7	0.3	0.7	230	50	0.294	0.020	0.564	0.194
8	0.3	0.8	240	10	0.290	0.033	0.902	0.128
9	0.3	0.7	230	10	0.300	0.000	0.702	0.003
10	0.2	0.6	240	30	0.200	0.000	0.498	0.170
11	0.3	0.7	250	50	0.296	0.013	0.623	0.110
12	0.2	0.7	240	50	0.204	0.020	0.569	0.187
13	0.4	0.7	250	30	0.406	0.015	0.725	0.036
14	0.3	0.7	250	10	0.297	0.010	0.770	0.100

Table 2. Cont.

Sd	Factors				Responses			
	L _t (mm)	R _w (mm)	E _t (°C)	P _s (mm/s.)	L _t (mm)	L _t Error	R _w (mm)	R _w Error
15	0.3	0.6	240	50	0.304	0.013	0.516	0.140
16	0.2	0.7	250	30	0.201	0.005	0.673	0.039
17	0.4	0.7	240	50	0.401	0.003	0.611	0.127
18	0.2	0.8	240	30	0.202	0.010	0.806	0.008
19	0.3	0.8	240	50	0.295	0.017	0.756	0.055
20	0.3	0.7	240	30	0.304	0.013	0.670	0.043
21	0.3	0.8	230	30	0.303	0.010	0.801	0.001
22	0.4	0.7	230	30	0.404	0.010	0.656	0.063
23	0.4	0.8	240	30	0.401	0.003	0.858	0.072
24	0.4	0.7	240	10	0.402	0.005	0.758	0.083
25	0.4	0.6	240	30	0.405	0.012	0.540	0.100
26	0.3	0.6	230	30	0.306	0.020	0.493	0.178
27	0.3	0.6	250	30	0.303	0.010	0.552	0.080
				Mean Error	0.011	Mean Error	0.080	

The effect of the four parameters, layer thickness, extruder temperature, printing speed, and raster width, on the dimensions was observed in Figure 5, revealing distinct trends in virtual thickness and width. The impact on width is more significant due to greater sensitivity to parameter variations, as evidenced by a wider range of width measurements, compared to the relatively stable thickness.

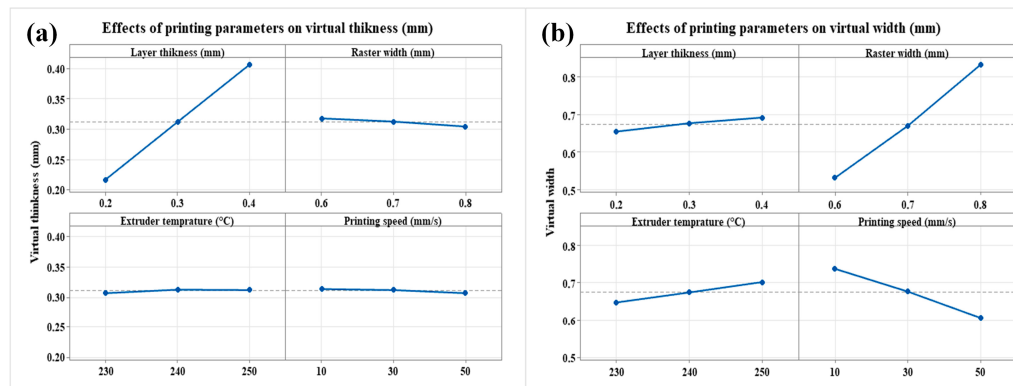


Figure 5. Effect of the printing parameter on the dimensions of virtual section, (a) virtual thickness (b) virtual width.

Figure 5a illustrates that the virtual thickness rises linearly with layer thickness. Thus, for a given layer thickness, the virtual thickness of the printed object remains constant. Other print options, such as raster width, extruder temperature, and print speed, do not significantly affect the virtual thickness. These parameters mainly influence the shape and surface quality of the printed object, but do not have a direct impact on the thickness of the deposited material. Therefore, it is possible to consider the virtual thickness to be equal to the layer thickness for the described printing parameter.

The virtual width is influenced by several print parameters, as shown in Figure 5b. It increases with layer thickness due to increased material spreading for thicker layers, and increases with increasing raster width, as this promotes material spreading. On the other hand, it decreases with higher extruder temperature, because a more fluid material is less likely to spread. Finally, the virtual width increases with print speed, as a higher speed reduces deposition time and leaves less time for the material to spread before solidification.

The virtual thickness error of 1.06% suggests a high degree of precision when compared to experimental data, however the width error of 8% indicates middling accuracy, likely driven by numerous interactions among process parameters. These discoveries, combined into the interface's shape generator, enable for exact modification of internal geometry during G-code parsing.

The reported "virtual thickness error" of 1.06% and "virtual width error" of 8% were calculated as the mean absolute percentage error across all 27 Box-Behnken experimental runs. Specifically, the error for each run was computed using the formula: Error = |Repose Value – Factor Value| / Factor Value.

Mathematical formula (1) provides an approximate calculation of the virtual width based on these parameters, significantly improving the accuracy of the Abaqus script generated by the interface.

$$V_w = 2.23 - 3.9L_t - 5.6 \times 10^{-1}R_w - 1.43 \times 10^{-2}E_t + 6.8 \times 10^{-3}P_s - 1.29 \times 10^{-1}L_t^2 + 1.196R_w^2 + 2.2 \times 10^{-5}E_t^2 - 6 \times 10^{-6}P_s^2 + 2.5 \times 10^{-1}L_t \times R_w + 1.675 \times 10^{-2}L_t \times E_t - 1.13 \times 10^{-3}L_t \times P_s + 2.50 \times 10^{-3}R_w \times E_t - 9.5 \times 10^{-3}R_w \times P_s - 1.1 \times 10^{-6}E_t \times P_s \quad (1)$$

With

- V_w : Virtual width (mm);
- L_t : Layer thickness (mm);
- R_w : Raster width (mm);
- E_t : Extruder temperature (°C);
- P_s : Printing speed (mm/s).

The model demonstrates excellent overall fit with an R^2 value of 98.85% (95% confidence interval: 97.6–99.5%), indicating that the model explains nearly all of the variability in the virtual width measurements. The adjusted R^2 of 97.51% accounts for the number of predictors in the model, confirming robust explanatory power without overfitting. The predicted R^2 of 93.39% further validates the model's strong generalizability to new observations, while the standard error of 0.018 mm represents high precision in virtual width prediction. The model F-value of 73.82 ($p < 0.001$) confirms high statistical significance, though individual components (linear, quadratic, and interaction effects) were not statistically significant, suggesting that the complete model's significance arises from the combined effect of all parameters rather than individual contributions. This robust statistical foundation supports the model's reliability for predicting virtual width in FDM simulations.

The interaction plot for virtual width presented on Figure 6 illustrates how key printing parameters, layer thickness, raster width, extruder temperature, and printing speed affect the actual width of extruded filaments in FDM 3D printing. As layer thickness and raster width increase, the virtual width rises due to greater material spreading. Conversely, higher extruder temperatures reduce width by improving material flow and reducing sagging. Printing speed also increases virtual width, as faster deposition limits the time available for spreading before solidification. The non-parallel lines across the subplots indicate significant interactions between these variables, highlighting that their effects are not independent. This confirms the need for a calibrated mathematical model to accurately predict filament geometry, which is essential for enhancing the fidelity of finite element simulations in Abaqus.

Ensuring the alignment between the refined virtual cross-section and the G-code path is crucial for ensuring that the Abaqus simulation accurately represents the physical Fused Deposition Modeling (FDM) process. The shape generator interprets the Infill Angle parameter (0° , 45° , 90°) by rotating the corrected virtual section's local coordinate system relative to the global build plate. As illustrated in Figure 7, the integration of the corrected filament section into the G-code path is demonstrated. The blue line denotes the G-code route

retrieved from the slicing program, controlling the motion of the altered virtual segment throughout the generation process. The red outline illustrates the revised virtual filament section, derived through significant experimental testing and computational modifications to more properly correlate with the physical deposition behavior. Centrally, the virtual model generation is demonstrated, stressing the seamless merging of experimental data into the computer model.

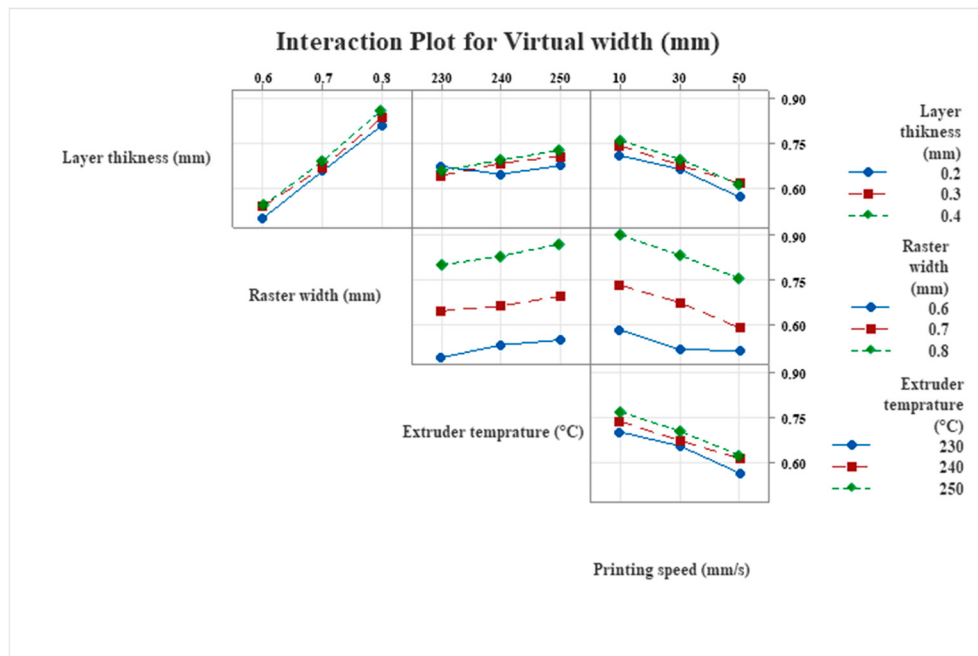


Figure 6. Interaction plot for Virtual width (mm).

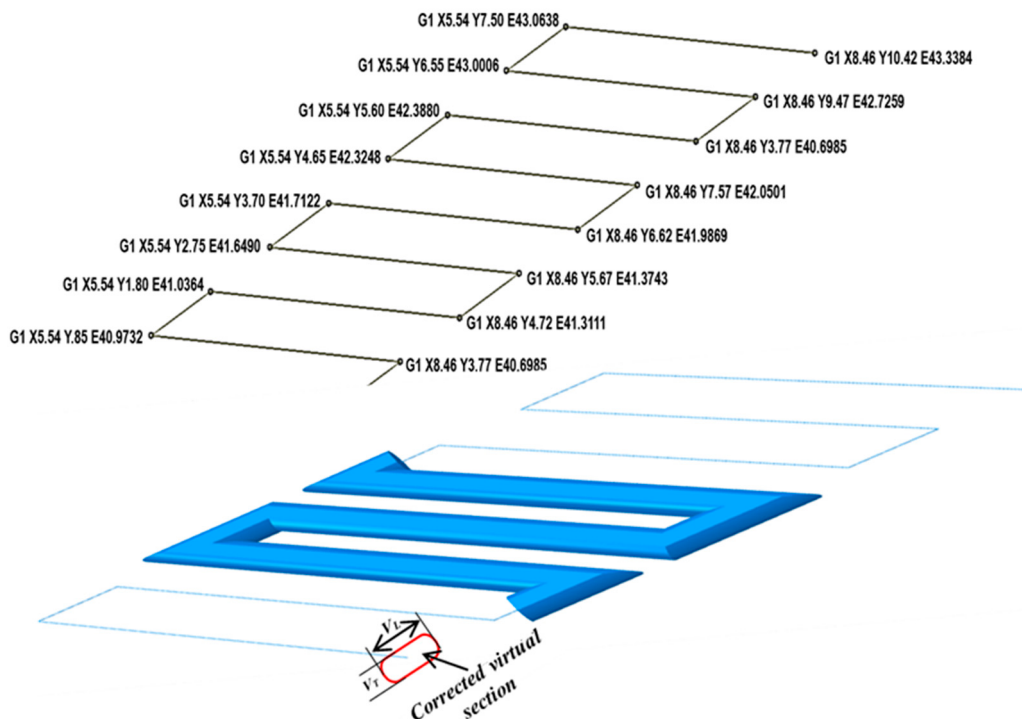


Figure 7. Integration of corrected virtual section (red) along G-code toolpath (blue).

2.4. Interface Development

The proposed solution introduces a specialized interface designed to seamlessly convert G-code into a format compatible with Abaqus, enabling advanced 3D printing simulations.

The interface, as illustrated in Figure 8, is embodied in the “Abaqus Script Generator from G-Code” tool, which features a streamlined and user-friendly design. It includes a file selection section where users can browse and upload a G-code file (.g), ensuring direct integration of printer instructions into the simulation environment. Additionally, the interface provides an “Infill Angle” input field, allowing users to specify angles such as 0°, 45°, or 90°, which gives the initial start to the corrected virtual section and adjusts the internal structure of the printed specimen for simulation purposes, ensuring precise mapping of G-code data to Abaqus’s event series framework for accurate simulations. A “Generate Abaqus Script” button triggers the conversion process, producing a script tailored for Abaqus to model the layer-by-layer deposition sequence.

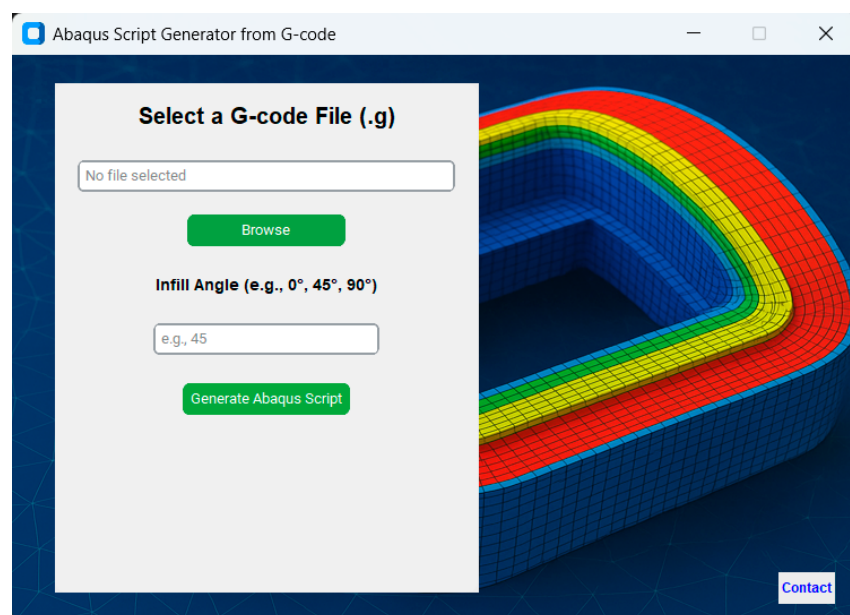


Figure 8. User Interface for G-Code to Abaqus Script Conversion.

The interface was developed in Python 3.8 using an interactive compiler environment for rapid prototyping and debugging. The final code was integrated into Visual Studio Code v1.104.0, linked directly to the Abaqus Python API (Abaqus Scripting Interface) via the Abaqus CAE kernel. This integration allows the tool to generate native Abaqus Python (.py) scripts that automatically construct the geometry, assign material properties, define meshing parameters.

2.5. Specimen Preparation and Testing

For the validation, two types of tensile tests were conducted: (i) tests on standard specimens and (ii) a complementary test on a single extruded filament.

ASTM D638 specimens. To compare numerical predictions with mechanical response, specimens were prepared according to the ASTM D638 Type V standard. Nine specimens were printed in total, divided into three groups corresponding to raster orientations of 0°, 45°, and 90° (three specimens per orientation to ensure reproducibility). All specimens were manufactured from ABS using a FlashForge Creator 3 PRO printer by Zhejiang Flashforge 3D Technology Co., Ltd. Jinhua, Zhejiang, China. The slicing was performed with FlashPrint v5.8.3 software, with the following parameters: layer height = 0.2 mm, nozzle diameter = 0.4 mm, nozzle temperature = 250 °C, bed temperature = 80 °C, and

print speed = 60 mm/s. A rectilinear infill with 100% density was applied to eliminate voids. Tensile tests were carried out on an MTS CRITERION MODEL 44 universal testing machine , MTS Systems Corporation Eden Prairie, Minnesota, United States, at room temperature under displacement control, following the ASTM procedure (Figure 9). Force and crosshead displacement were recorded continuously, and engineering stress–strain curves were derived for each specimen.

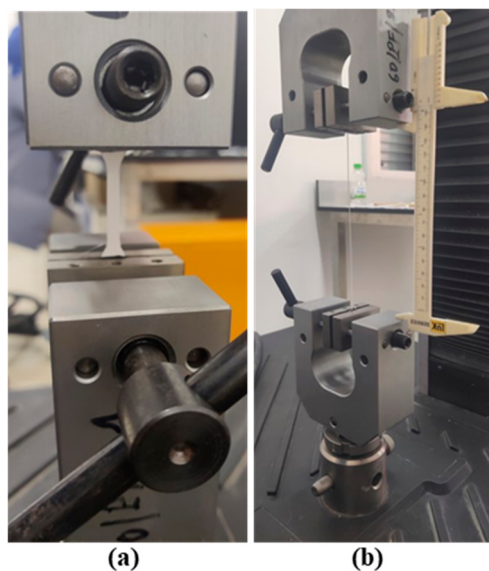


Figure 9. Tensile test setup: (a) ASTM D638 Type V specimens printed at 0°, 45°, and 90° raster orientations; (b) monofilament specimen prepared with 145 mm length and 0.4 mm diameter, mounted in a custom fixture to avoid slippage.

Monofilament test. To characterize the geometry and mechanical response of a single extruded filament, a dedicated tensile test was performed on one filament sample. The filament was prepared with a length of 145 mm and a diameter of approximately 0.4 mm, extruded directly by the same printer and process parameters as the D638 specimens. The ends of the filament were carefully clamped in a custom-designed fixture, which was in turn mounted onto the MTS machine. Mechanical grips and additional clamps were used to minimize slippage and ensure proper load transfer during testing.

For the second part of the experiment, Tensile tests on the filaments were conducted using a specialized support designed to hold them in place during testing. The mechanical properties of the filaments are detailed in Table 3 and are injected into Abaqus as mechanical properties for simulation.

Table 3. Mechanical Properties of Monofilament for Tensile Testing.

Properties	Unit	Value
Yield strength	MPa	45
Ultimate Stress	MPa	65
Elongation at Break	-	0.05
Young's Modulus	MPa	2190
Poisson's Ratio	-	0.34
Density	Kg/m ³	1010

3. Results and Discussion

3.1. Comparative Analysis of Geometries

This section validates the geometric fidelity of our tool by comparing the 3D structures generated in Abaqus (after G-code processing) against the intended geometries embedded in the original slicer-generated G-code.

Figure 10 displays two rows of specimens, with the top row representing the geometries generated by the Abaqus simulation using my tool, and the bottom row showing the geometries directly generated by the slicer from the G-code. The consistent alignment and similarity between the two rows indicate that my tool accurately captures the overall shape and geometry of the specimens as intended by the G-code instructions. Each column in the image corresponds to a different infill pattern and density configuration, and the internal structures of the specimens, whether they are honeycomb, grid, or linear infills, are faithfully replicated in both the Abaqus simulation and the slicer-generated geometries. This precise matching demonstrates that my tool effectively interprets the G-code to reproduce complex infill patterns with high fidelity.

		<i>Slicer result</i>	<i>Numerical result</i>
<i>Density</i>	20%		
	60%		
	100%		
<i>Orientation</i>	(0°/90°)		
	(45°/-45°)		
	(90°/0°)		
<i>External layer</i>	One		
	Two		
	Three		
<i>Infill pattern</i>	Honeycomb (Hexagonal)		
	Linear		
	Gyroid (3D)		
	Triangular		

Figure 10. Comparison of Abaqus Simulation and Slicer-Generated Geometries.

The specimens manifest equivalent wall layers, infill densities, and orientations across both the Abaqus simulation and the slicer-generated geometries, thereby substantiating

the tool's dependability in converting G-code instructions into precise Abaqus geometries without compromising the intricacies or structural integrity of the original design. The image reveals no significant differences between the corresponding specimens from the two sources, suggesting that the tool adeptly minimizes potential errors or variations during the conversion process. This approach guarantees that the simulation models accurately replicate the actual printed objects. The precise geometric alignment serves to substantiate the program's functionality and precision. This finding suggests that the model can be used to make predictions in Fused Deposition Modeling (FDM) processes, which lends credibility to the model. The comparative study shows the robust capacity of my developed tool to convert G-code instructions into Abaqus geometries with excellent precision, reinforcing its promise as a significant resource for developing the mechanical analysis and simulation of FDM-printed parts.

As shown in Figure 11, a comparative analysis of a spherical specimen's geometry is provided. This analysis is based on the geometry of the specimen, as generated by the developed tool and the slicer. The top image illustrates the geometry produced by the slicer from the G-code instructions, while the bottom image displays the geometry generated by the Abaqus simulation using the developed tool. The perfect matching and consistent layering across both representations highlight the tool's ability to precisely interpret G-code directives and faithfully recreate complex geometries within Abaqus. A comparative analysis of the two images shows that they share identical layer stacking, curvature, and surface intricacies. This finding confirms that the developed tool effectively captures the detailed features of the spherical specimen. For instance, the consistent radial coordinates and angular alignment in both models demonstrate that the tool accurately replicates the intended spherical dimensions, with layer heights matching precisely. This precise replication of the slicer's output in the Abaqus simulation demonstrates the tool's effectiveness in converting G-code instructions into accurate simulation geometries, maintaining consistency in layer height, shape, and internal structures.

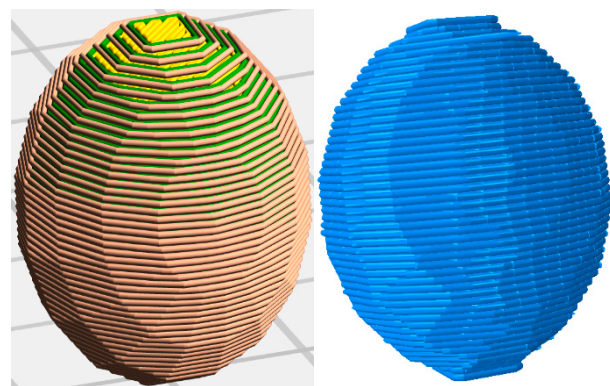


Figure 11. Comparative Analysis of Spherical Specimen Geometry—Slicer vs. Abaqus Simulation.

A comparative visualization of a NACA duct geometry, a sophisticated aerodynamic structure widely utilized in aerospace applications, is presented in Figure 12, produced by both a slicer and a custom-developed tool. The interface of the developed tool displays a carefully layered construction featuring smooth curvature. The perspective view shows the tool's capability and efficiency in capturing the internal layering with precision and accurate infill patterns, showcasing its ability to reliably interpret G-code instructions. This high-capability for regeneration shows the tool's dependability for simulating complex designs, aligning effortlessly with the output of the slicer, which fill the gap between design and thermomechanical analysis with precision.

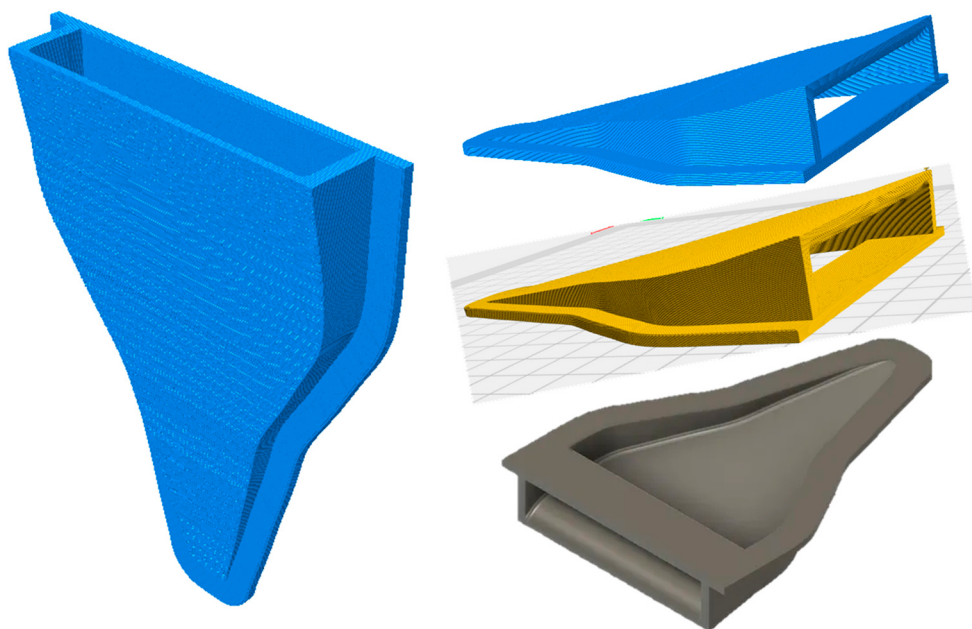


Figure 12. Comparative Visualization of NACA Duct Geometry—Slicer vs. Developed Tool.

Figure 13 illustrates the analysis of filament interactions. The program excels in the analysis of the interaction between filaments, which is considered an essential factor in studying crack propagation, with the central configuration (“Only Theoretical”) presenting an idealized theoretical model of uniformly stacked green filaments overlaid with orange and green intertwined networks to symbolize potential interactions, this model does not reflect a real shape, it is an ideal representation, whereas in reality the filament flattens underweight and pressure. The right configuration demonstrates a well-defined extrusion at 0.2 mm layer height, 100% infill, 60 mm/min speed, and 250 °C nozzle temperature, overlapping blue filaments, indicating strong cohesion and structural integrity, suggesting a desirable outcome in material analysis. In contrast, the left configuration at 0.4 mm layer height, 100% infill, 60 mm/min speed, and 250 °C nozzle temperature, shows filaments that are less flattened with a weaker interaction zone, implying reduced cohesion and a potential vulnerability to crack propagation. The diagram highlights filament interaction analysis by comparing two configurations against a central theoretical model.

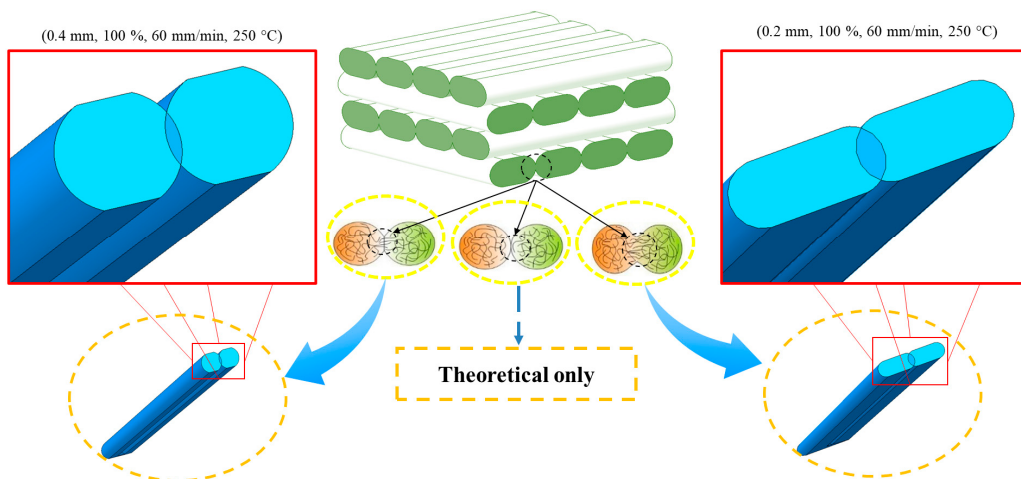


Figure 13. Analysis of Filament Interactions—Theoretical vs. Experimental Configurations.

The average overlap percentage was 98.3% ($SD = 0.7\%$), with the lowest value of 97.1% for the most complex NACA duct geometry. The mean surface deviation of

0.018 mm ($SD = 0.005$ mm). The Dice similarity coefficient averaged 0.992 ($SD = 0.003$) across all test cases. The maximum Harsdorf distance was 0.047 mm, well below the 0.1 mm threshold for FDM simulation accuracy. These metrics confirm that our tool maintains exceptional geometric fidelity while converting G-code to Abaqus geometries.

Figure 14 shows a comparative meshed visualization of an ASTM D638 specimen and a NACA duct a geometry based on the NACA 0012 airfoil profile, which are meshed using varying dimensions to illustrate the proficiency of the developed program in generating and adapting meshes for various structures. The image highlights the program's versatility and flexibility of the program, using C3D4 mesh elements with adapted sizes (0.35 to 0.6) depending on the geometrical complexity of the structures.

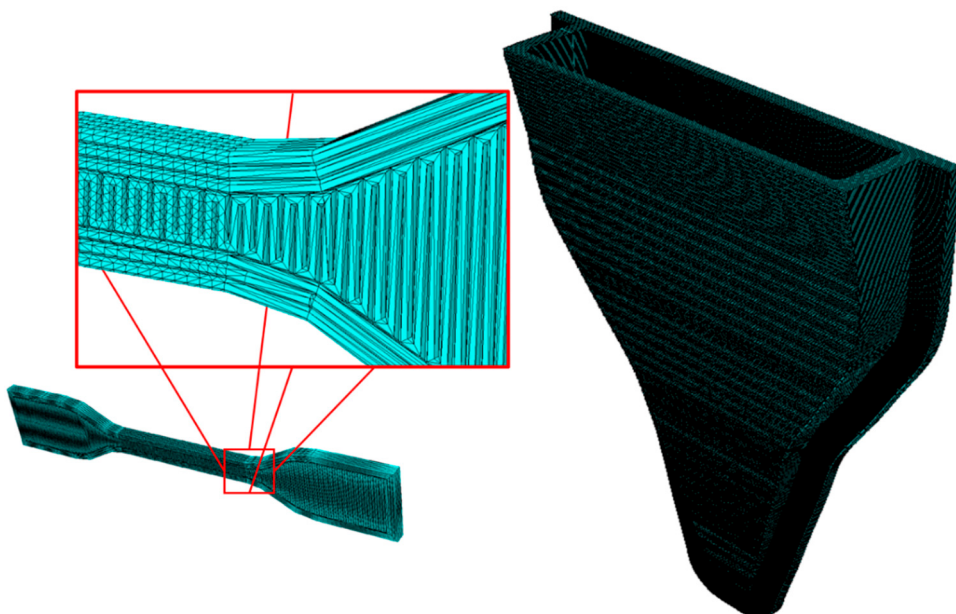


Figure 14. ASTM D638 and NACA Duct Meshes.

The zoomed-in area to the left is the ASTM D638 specimen, which shows the internal layers fine meshed area that demonstrates the capability of the program to accurately replicate complex patterns without compromising the integrity of the structure. The NACA duct, a complex aerodynamic structure, is presented on the right side, with a coarser mesh that adapts to its contoured, stratified shape, demonstrating the tool's ability to refine mesh density according to structural requirements. The two views together draw attention to the software's success in generating high-fidelity meshes for application in a range of scenarios, from tensile test standards to aerodynamics simulations.

3.2. Numerical Model Validation

The experimental tensile curves presented in Figure 15 reveal varying behavior depending on the filament orientation. At 90° , the material exhibits plasticity with brittle fracture. At 0° , it achieves a maximum tensile strength of 41.42 MPa, indicating ductile fracture. At 45° , the behavior is intermediate, with an average tensile strength of 38.22 MPa and ductile fracture.

The numerical tensile testing was carried out on two series of ASTM D638 samples: one with an uncorrected virtual section and another with the corrected virtual section. The dimensions of the virtual section were maintained constant along the entire length of the virtual raster, providing a stable framework for the simulation. Perfect bonding between filaments and layers was assumed, simplifying the model by eliminating variables related to imperfect interlayer adhesion. The assumption of perfect interlayer bonding was

adopted to isolate the geometric effects of filament cross-section correction from the complex thermomechanical phenomena of interlayer adhesion. All simulations were conducted at room temperature to standardize environmental conditions and avoid thermal variability. The build platform temperature was assumed to have negligible impact on mechanical behavior. This approach follows the methodology of Hachimi et al. [19] who demonstrated that geometric accuracy has a more significant impact on simulation fidelity than minor variations in material properties for the initial validation phase.

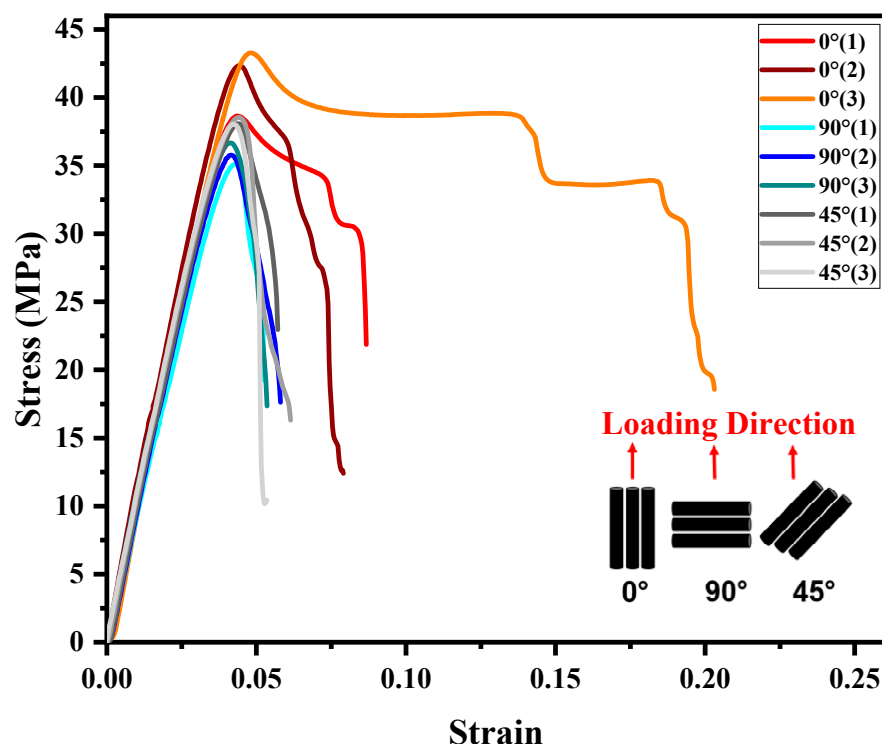


Figure 15. Tensile Stress–Strain Curves for ASTM D638 Specimens at 0° , 45° , and 90° Orientations.

The mechanical properties of the ABS monofilament were assumed to remain unchanged during extrusion, ensuring consistent material behavior throughout the simulation. The assumption of constant material properties during extrusion was made to focus on the geometric fidelity of the virtual section model, as the mechanical properties were measured from the monofilament test (Table 3) representing the material after solidification.

Figure 16 illustrates the numerical tensile test setup in Abaqus for ASTM D638 specimens at 0° , 45° , and 90° orientations. The meshed model shows one end fixed ("Encastred") and the opposite end subjected to a displacement-controlled load along the longitudinal axis. The displacement magnitude was determined from experimental tensile tests to ensure alignment with real-world conditions. The selection of C3D4 linear tetrahedral elements and the element size range of 0.35–0.6 mm was determined through a systematic mesh convergence study. Simulations were performed with element sizes from 1.0 mm down to 0.35 mm; a size of 0.55 mm was selected globally as it yielded less than 2% variation in maximum tensile stress compared to finer meshes, balancing accuracy and computational cost. In geometrically complex, the mesh was locally refined to 0.35 mm, while uniform regions used 0.6 mm elements implementing a region-based adaptive strategy. While C3D4 elements are known to exhibit reduced accuracy in capturing stress concentrations and highly nonlinear material behavior due to their constant strain formulation, they were chosen for their robustness in meshing irregular, toolpath-derived geometries a critical requirement for G-code-based simulations.

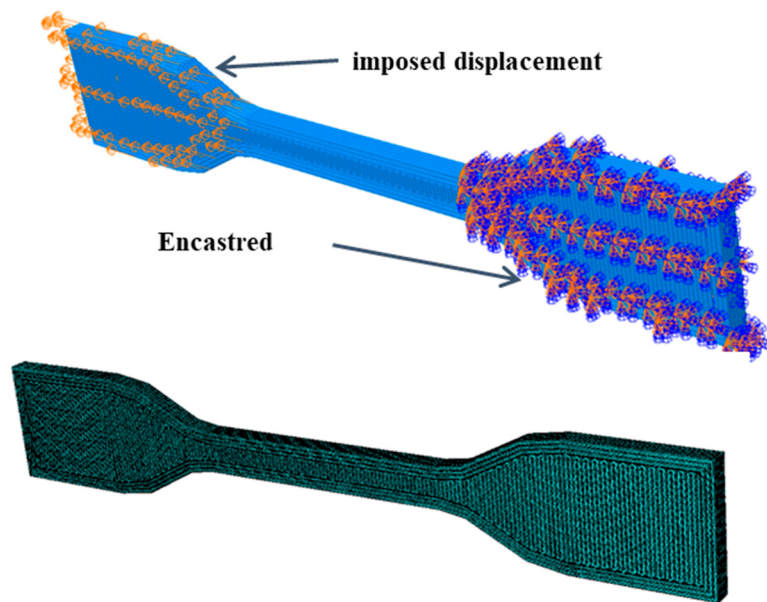


Figure 16. Numerical Tensile Meshing of ASTM D638 Specimens in Abaqus.

3.3. Tensile Test Comparison

Figure 17 presents a comparative mechanical analysis of stress–strain curves from numerical tensile tests of ASTM D638 specimens, conducted using the developed program, alongside representative experimental tensile curves across three filament orientations: 0° (a), 45° (b), and 90° (c). Each subplot includes four curves: three experimental datasets labeled “Experimental (1)” in green, “Experimental (2)” in teal, and “Experimental (3)” in olive, representing multiple trials, representing typical test data. Two numerical simulation results are included: “Numerical test (Corrected)” marked with blue circles and “Numerical test (non-Corrected)” marked with red triangles.

For all orientations 0° , 45° , and 90° , the experimental curves exhibit a characteristic ductile behavior, featuring an initial linear elastic region followed by a nonlinear plastic region, indicative of yielding and strain hardening. Across the orientations reveals distinct mechanical behaviors: the 0° orientation has the highest tensile strength and ductility, likely due to aligned filament layers maximizing load-bearing capacity. The 45° orientation shows an intermediate mechanical property, with reduced strength and ductility attributed to the angled filament arrangement, which introduces shear stresses, the 90° orientation takes the tensile strength and a more brittle response, as perpendicular filaments are less effective at resisting longitudinal tensile forces, leading to earlier failure. These differences underscore the impact of filament orientation on mechanical properties.

The “Numerical test (Corrected)” curve follows the experimental data closely in both the elastic and initial plastic zone, indicating improved accuracy through the corrected section model, which more accurately simulates filament cohesion and stress distribution. Conversely, the “Numerical test (non-Corrected)” curve deviates more, especially in the plastic zone, indicating potential underestimation of ductility and tensile strength as a result of the uncorrected section’s inability to capture realistic filament behavior. Also included in each subplot is the color-coded stress distribution map of the specimen, which visually represents the concentration of stress. The simulation across all orientations shows the enhanced agreement of the corrected model with experimental observation, thus enhancing the prediction of mechanical properties like yield strength and ultimate tensile strength, and verifying its efficacy in optimizing the design and performance of 3D-printed components.

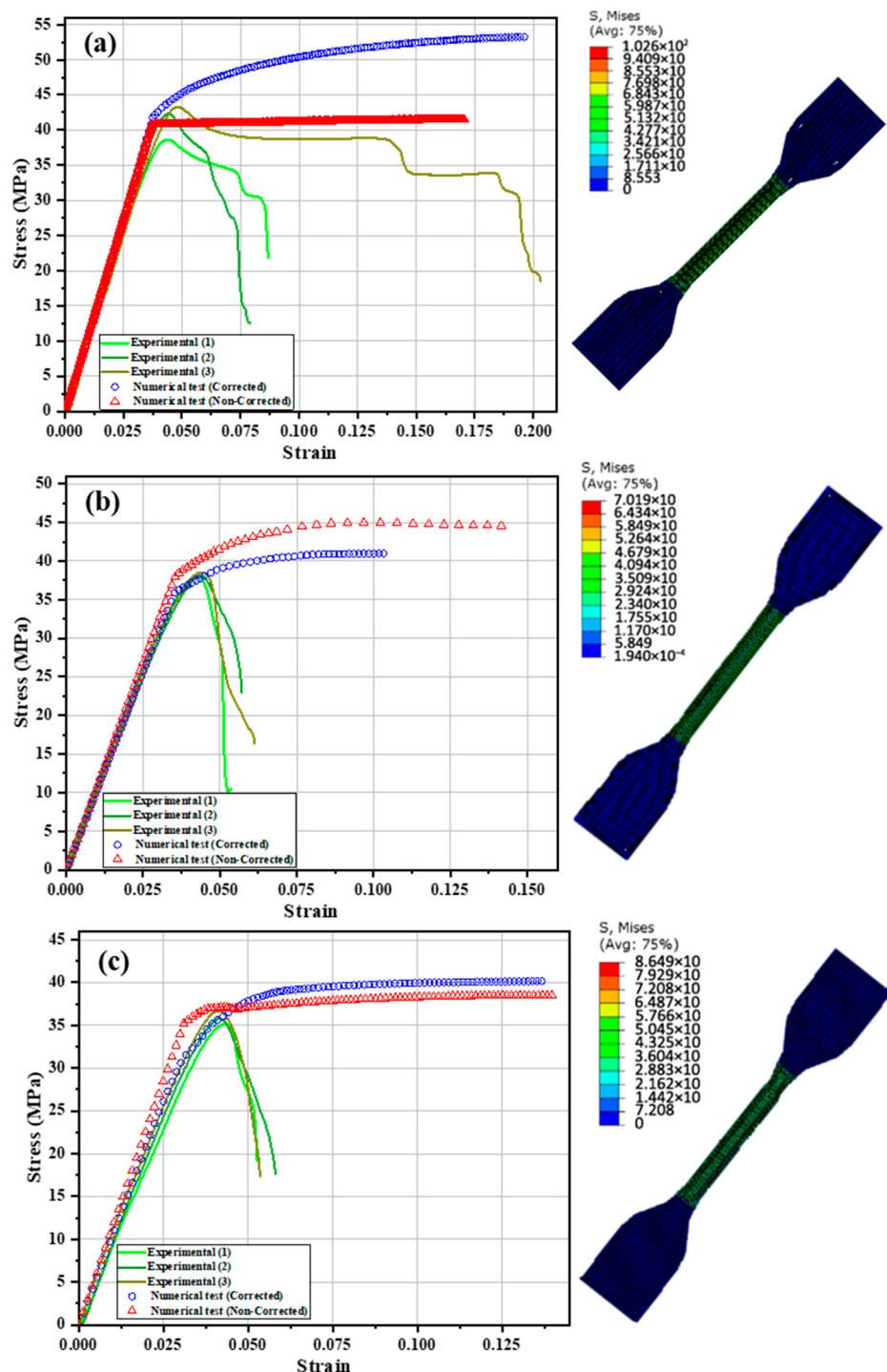


Figure 17. Comparative Stress–Strain Curves and Stress Distribution of ASTM D638 Specimens for (a) 0°, (b) 45°, and (c) 90° Orientations—Corrected vs. Non-Corrected Numerical Models with the experimental result.

Initially, the uncorrected section samples showed a reasonable correlation with experimental data, indicating a sound foundation for the simulation technique. However, the new section results in simulation findings that more closely resemble actual tensile test results, thereby improving the model's accuracy. This is because the corrected section model better captures the interactions of filaments and the distribution of stress, thereby enabling the simulation to more realistically follow the behavior of the specimen. The analysis underscores the instrument's capability to enhance mesh configurations, markedly augmenting

the correlation between simulated and experimental findings, thereby substantiating the efficacy of the amended section in advancing simulation accuracy.

For the 90° orientation specimens, the mechanical behavior exhibited a more brittle response compared to the 0° and 45° orientations, as evidenced by the reduced ductility and earlier failure. The corrected virtual section model demonstrated strong agreement with experimental results, achieving $R^2 = 0.9833$ with RMSE = 0.90 MPa. The coefficient of variation (%CV) across the three replicates was 3.5%, for 45° achieving $R^2 = 0.9987$ with RMSE = 0.20 MPa. The coefficient of variation (%CV) across the three replicates was 2.3% and for 0° achieving $R^2 = 0.9210$ with RMSE = 0.47 MPa. The coefficient of variation (%CV) across the three replicates was 5.2% which, while higher than the other orientations, remains within an acceptable range for preliminary validation. The model accurately captured both the elastic behavior ($R^2 = 0.955$ in strain <0.012) and the transition to failure, with the stress distribution map in Figure 17c confirming that failure initiates at the expected location for perpendicular filament arrangements. These statistical metrics were calculated by comparing the corrected simulation results to the mean value of the three experimental curves.

Our Box-Behnken-based modeling approach achieves correlation coefficients exceeding 95% in the elastic zone and 90% in the elastoplastic zone performance metrics that align with, and in some aspects exceed, recent optimization studies using alternative DOE methods. For instance, Kechagias [32] employed Taguchi L25 design to optimize flexural strength in ABS FDM prints and reported significant parameter rankings (infill density, raster angle) but did not quantify simulation-to-experiment correlation. Our approach explicit modeling of quadratic effects and parameter interactions (layer thickness \times temperature), which Taguchi's linear-additive model cannot capture without sacrificing orthogonality, and direct output of a predictive equation (Equation (1)) for virtual geometry. As Kechagias himself notes, "quadratic models can possibly be used in Taguchi but are not recommended".

The modified section improves filament adhesion and stress distribution, which may lead to an increase in tensile strength, whereas the unmodified section demonstrates less robust interaction zones, suggesting a susceptibility to failure when subjected to load.

4. Conclusions

This study introduces an integrated, experimentally validated workflow that converts FDM printer G-code into high-fidelity Abaqus simulations by correcting the virtual raster section for filament deformation. The core innovation lies in a Box-Behnken-calibrated mathematical model that predicts the true oval-rectangular cross-section of extruded filaments achieving only 1.06% thickness error and 8% width error replacing idealized circular assumptions. Coupled with a Python-based shape generator, this enables automated creation of mesh-ready Abaqus models that accurately replicate complex infill patterns and orientations.

Validation via tensile testing of ASTM D638 specimens (0°, 45°, 90°) confirms the model's effectiveness: simulations using the corrected section achieved >95% correlation in the elastic regime and >90% in the elastoplastic regime significantly outperforming uncorrected models. This demonstrates a substantial leap in predicting anisotropic mechanical behavior directly from printer settings.

Key limitations include assumptions of perfect interlayer bonding and validation limited to ABS on a single printer. Thermal history and residual stresses were not modeled.

Future work will extend the framework to multi-material prints, incorporate real-time thermal data, and generalize the tool for broader slicer and printer compatibility. By transforming G-code from machine instructions into physics-informed simulation inputs,

this tool provides a foundational step toward reliable, predictive digital twins for FDM-printed components in aerospace, medical, and automotive applications.

Author Contributions: Study conception and design: T.H., F.A.H., F.E.A., and H.R.; Data collection: T.H., F.A.H., F.E.A., and H.R.; Analysis and interpretation of results: T.H., F.A.H., F.E.A., and H.R.; Draft manuscript preparation, methodology, resources, and editing: T.H.; Supervision, validation, visualization, methodology, resources, review, and editing: Y.R., and F.M. All authors have read and agreed to the published version of the manuscript.

Funding: This research received no external funding.

Data Availability Statement: The data are available on request.

Conflicts of Interest: The authors declare no conflicts of interest.

Abbreviations

The following abbreviations are used in this manuscript:

AM	Additive Manufacturing
FDM	Fused Deposition Modeling
FEA	Finite Element Analysis
SEM	Scanning Electron Microscopy

References

- Gibson, I.; Rosen, D.; Stucker, B.; Khorasani, M.; Rosen, D.; Stucker, B.; Khorasani, M. *Additive Manufacturing Technologies*; Springer: Berlin/Heidelberg, Germany, 2021; Volume 17.
- Mishra, V.; Negi, S.; Kar, S. FDM-Based Additive Manufacturing of Recycled Thermoplastics and Associated Composites. *J. Mater. Cycles Waste Manag.* **2023**, *25*, 758–784. [[CrossRef](#)]
- Hachimi, T.; Ait Hmazi, F.; Majid, F. Damage of Additively Manufactured Polymer Materials: Experimental and Probabilistic Analysis. *Fract. Struct. Integr.* **2025**, *19*, 236–255. [[CrossRef](#)]
- Fidan, I.; Huseynov, O.; Ali, M.A.; Alkunte, S.; Rajeshirke, M.; Gupta, A.; Hasanov, S.; Tantawi, K.; Yasa, E.; Yilmaz, O.; et al. Recent Inventions in Additive Manufacturing: Holistic Review. *Inventions* **2023**, *8*, 103. [[CrossRef](#)]
- Naboulsi, N.; Majid, F.; Hachimi, T.; Dadoun, S.; Barhoumi, N.; Khelifi, K. Predicting the Strength of 3D-Printed Conductive Composite under Tensile Load: A Probabilistic Modeling and Experimental Study. *Fract. Struct. Integr.* **2025**, *19*, 247–262. [[CrossRef](#)]
- Pereira, T.; Kennedy, J.V.; Potgieter, J. A Comparison of Traditional Manufacturing vs Additive Manufacturing, the Best Method for the Job. *Procedia Manuf.* **2019**, *30*, 11–18. [[CrossRef](#)]
- du Plessis, A.; Razavi, N.; Benedetti, M.; Murchio, S.; Leary, M.; Watson, M.; Bhate, D.; Berto, F. Properties and Applications of Additively Manufactured Metallic Cellular Materials: A Review. *Prog. Mater. Sci.* **2022**, *125*, 100918. [[CrossRef](#)]
- Segovia-Guerrero, L.; Baladés, N.; Gallardo-Galán, J.J.; Gil-Mena, A.J.; Sales, D.L. Additive vs. Subtractive Manufacturing: A Comparative Life Cycle and Cost Analyses of Steel Mill Spare Parts. *J. Manuf. Mater. Process.* **2025**, *9*, 138. [[CrossRef](#)]
- Suresh, V.; Balasubramaniam, B.; Yeh, L.H.; Li, B. Recent Advances in In Situ 3D Surface Topographical Monitoring for Additive Manufacturing Processes. *J. Manuf. Mater. Process.* **2025**, *9*, 133. [[CrossRef](#)]
- Alami, A.H.; Ghani Olabi, A.; Alashkar, A.; Alasad, S.; Aljaghoub, H.; Rezk, H.; Abdelkareem, M.A. Additive Manufacturing in the Aerospace and Automotive Industries: Recent Trends and Role in Achieving Sustainable Development Goals. *Ain Shams Eng. J.* **2023**, *14*, 102516. [[CrossRef](#)]
- Picard, M.; Mohanty, A.K.; Misra, M. Recent Advances in Additive Manufacturing of Engineering Thermoplastics: Challenges and Opportunities. *RSC Adv.* **2020**, *10*, 36058–36089. [[CrossRef](#)] [[PubMed](#)]
- Pal, A.K.; Mohanty, A.K.; Misra, M. Additive Manufacturing Technology of Polymeric Materials for Customized Products: Recent Developments and Future Prospective. *RSC Adv.* **2021**, *11*, 36398–36438. [[CrossRef](#)]
- Duong, T.H.; Jaksic, N.I.; Depalma, J.L.; Ansaf, B.; Daniel, D.M.; Armijo, J.; Galaviz, M. G-Code Visualization and Editing Program for Inexpensive Metal 3D Printing. *Procedia Manuf.* **2018**, *17*, 22–28. [[CrossRef](#)]
- Bacciaglia, A.; Falchetto, F.; Troiani, E.; Di Sante, R.; Liverani, A.; Ceruti, A. Geometry Reconstruction for Additive Manufacturing: From G-CODE to 3D CAD Model. *Mater. Today Proc.* **2023**, *75*, 16–22. [[CrossRef](#)]

15. Rahman, K.M.; Letcher, T.; Reese, R. Mechanical Properties of Additively Manufactured PEEK Components Using Fused Filament Fabrication. In Proceedings of the ASME International Mechanical Engineering Congress and Exposition, Houston, TX, USA, 13–19 November 2015; American Society of Mechanical Engineers: New York, NY, USA, 2015; Volume 57359, p. V02AT02A009.
16. Abaqus Scripting User’s Manual. Abaqus 6.11. 2012, 89, v6. Available online: <http://abaqusdocs.eait.uq.edu.au/v6.11/index.html> (accessed on 11 August 2025).
17. Barbero, E.J. *Finite Element Analysis of Composite Materials Using Abaqus®*; CRC Press: Boca Raton, FL, USA, 2023; ISBN 1003108156.
18. Zouaoui, M.; Gardan, J.; Lafon, P.; Makke, A.; Labergere, C.; Recho, N. A Finite Element Method to Predict the Mechanical Behavior of a Pre-Structured Material Manufactured by Fused Filament Fabrication in 3D Printing. *Appl. Sci.* **2021**, *11*, 5075. [[CrossRef](#)]
19. Hachimi, T.; Zekriti, N.; Rhanim, R.; Rhanim, H.; Majid, F. Modeling and Simulation of the Influence of 3D Printing Parameters on Crack Propagation: Filament Orientation. In *Advanced Materials for Sustainable Energy and Engineering: Volume 1: Novel Nanomaterials for Sustainable Energy*; Boutahir, M., El Mehdi, E., Eds.; Springer Nature Switzerland: Cham, Switzerland, 2025; pp. 231–245. ISBN 978-3-031-75032-8.
20. Zouaoui, M.; Labergere, C.; Gardan, J.; Makke, A.; Recho, N.; Alexandre, Q.; Lafon, P. Numerical Prediction of 3d Printed Specimens Based on a Strengthening Method of Fracture Toughness. *Procedia CIRP* **2019**, *81*, 40–44. [[CrossRef](#)]
21. Zhang, Y.; Huang, X. Simulation and Research of Aerospace Material Milling Based On ABAQUS. *J. Phys. Conf. Ser.* **2020**, *1653*, 012070. [[CrossRef](#)]
22. Marrel, A.; Velardo, H.; Bouloré, A. Likelihood and Depth-Based Criteria for Comparing Simulation Results with Experimental Data, in Support of Validation of Numerical Simulators. *Int. J. Uncertain Quantif.* **2024**, *14*, 45–68. [[CrossRef](#)]
23. Nagarajan, H.P.N.; Mokhtarian, H.; Jafarian, H.; Dimassi, S.; Bakrani-Balani, S.; Hamed, A.; Coatanéa, E.; Gary Wang, G.; Haapala, K.R. Knowledge-Based Design of Artificial Neural Network Topology for Additive Manufacturing Process Modeling: A New Approach and Case Study for Fused Deposition Modeling. *J. Mech. Des.* **2019**, *141*, 021705. [[CrossRef](#)]
24. Brenken, B.; Barocio, E.; Favalo, A.; Kunc, V.; Pipes, R.B. Development and Validation of Extrusion Deposition Additive Manufacturing Process Simulations. *Addit. Manuf.* **2019**, *25*, 218–226. [[CrossRef](#)]
25. Favalo, A.J.; Brenken, B.; Barocio, E.; Pipes, R.B. Simulation of Polymeric Composites Additive Manufacturing Using Abaqus. *Sci. Age Exp.* **2017**, 103–114.
26. Talagani, M.R.; DorMohammadi, S.; Dutton, R.; Godines, C.; Baid, H.; Abdi, F.; Kunc, V.; Compton, B.G.; Simunovic, S.; Duty, C.E.; et al. Numerical Simulation of Big Area Additive Manufacturing (3D Printing) of a Full Size Car. *SAMPE J.* **2015**, *51*, 27–36.
27. Faria, C.; Fonseca, J.; Bicho, E. FIBR3DEmul—An Open-Access Simulation Solution for 3D Printing Processes of FDM Machines with 3+ Actuated Axes. *Int. J. Adv. Manuf. Technol.* **2020**, *106*, 3609–3623. [[CrossRef](#)]
28. Molazadeh, S.; Diba, F.; Hosseini, A. Anisotropic Modeling of Material Behavior for Additively Manufactured Parts Made by Material Extrusion. *Int. J. Adv. Manuf. Technol.* **2023**, *129*, 3453–3473. [[CrossRef](#)]
29. Timofeeva, O.S.; Andreev, Y.S.; Yablochnikov, E.I. Simulation of Injection Molding Process and 3D-Printing of Forming Parts for Small-Batch Production. In Proceedings of the 2019 IEEE 17th International Conference on Industrial Informatics (INDIN), Helsinki, Finland, 22–25 July 2019; Volume 1, pp. 1631–1637.
30. Dallal, S.; Eslami, B.; Tiari, S. Recent Advances in PEEK for Biomedical Applications: A Comprehensive Review of Material Properties, Processing, and Additive Manufacturing. *Polymers* **2025**, *17*, 1968. [[CrossRef](#)] [[PubMed](#)]
31. Hachimi, T.; Majid, F.; Zekriti, N.; Rhanim, R.; Rhanim, H. Improvement of 3D Printing Polymer Simulations Considering Converting G-Code to Abaqus. *Int. J. Adv. Manuf. Technol.* **2024**, *131*, 5193–5208. [[CrossRef](#)]
32. Kechagias, J.D. 3D Printing Parametric Optimization Using the Power of Taguchi Design: An Expository Paradigm. *Mater. Manuf. Process.* **2024**, *39*, 797–803. [[CrossRef](#)]

Disclaimer/Publisher’s Note: The statements, opinions and data contained in all publications are solely those of the individual author(s) and contributor(s) and not of MDPI and/or the editor(s). MDPI and/or the editor(s) disclaim responsibility for any injury to people or property resulting from any ideas, methods, instructions or products referred to in the content.